

# Evolution of X-ray activity of 1–3 $M_{\odot}$ late-type stars in early post-main-sequence phases

N. Pizzolato<sup>1</sup>, A. Maggio<sup>2</sup>, and S. Sciortino<sup>2</sup>

<sup>1</sup> Dipartimento di Scienze Fisiche ed Astronomiche, Università di Palermo, Sezione di Astronomia, Piazza del Parlamento 1, 90134 Palermo, Italy (nicola@oapa.astropa.unipa.it)

<sup>2</sup> Osservatorio Astronomico di Palermo, Piazza del Parlamento 1, 90134 Palermo, Italy (maggio@oapa.astropa.unipa.it)

Received 14 March 2000 / Accepted 7 July 2000

**Abstract.** We have investigated the variation of coronal X-ray emission during early post-main-sequence phases for a sample of 120 late-type stars within 100 pc, and with estimated masses in the range 1–3  $M_{\odot}$ , based on *Hipparcos* parallaxes and recent evolutionary models. These stars were observed with the ROSAT/PSPC, and the data processed with the Palermo-CfA pipeline, including detection and evaluation of X-ray fluxes (or upper limits) by means of a wavelet transform algorithm. We have studied the evolutionary history of X-ray luminosity and surface flux for stars in selected mass ranges, including stars with inactive A-type progenitors on the main sequence and lower mass solar-type stars. Our stellar sample suggests a trend of increasing X-ray emission level with age for stars with masses  $M > 1.5M_{\odot}$ , and a decline for lower-mass stars. A similar behavior holds for the average coronal temperature, which follows a power-law correlation with the X-ray luminosity, independently of their mass and evolutionary state. We have also studied the relationship between X-ray luminosity and surface rotation rate for stars in the same mass ranges, and how this relationship departs from the  $L_x \propto v_{\text{rot}}^2$  law followed by main-sequence stars. Our results are interpreted in terms of a magnetic dynamo whose efficiency depends on the stellar evolutionary state through the mass-dependent changes of the stellar internal structure, including the properties of envelope convection and the internal rotation profile.

**Key words:** stars: coronae – stars: late-type – X-rays: stars – stars: activity – stars: evolution

## 1. Introduction

Shortly after the discovery that stellar X-ray emission is ubiquitous in the H-R diagram (Vaiana et al. 1981), it has been recognized that such emission may be used as a diagnostic for processes affecting stellar evolution. In the specific case of late-type stars, X-ray emission signals the presence of magnetic fields which are relevant both for the heating of coronal plasma and for stellar mass and angular momentum losses, occurring during

most of a star’s life. In turn, the intensity and spatial distribution of magnetic fields are likely determined by a dynamo mechanism, whose mode of operation and efficiency depend on the interplay between stellar rotation and subphotospheric convective motions. Hence, the X-ray emission level and temperature of the coronal plasma may change in response to evolutionary changes of the star’s rotation and internal structure, and – from an observational point of view – X-ray emission can be used as a tool to investigate on the link between stellar coronae and stellar interiors.

This kind of study is particularly challenging for stars in the evolutionary phases across the Hertzsprung gap and on the giant branch, because of the relatively short time scales in which several effects take place: among the others, the development of a deep convection zone (even for stars lacking it while on the main-sequence), the rapid expansion of the stellar radius with the consequent increase of the moment of inertia and decrease of the surface gravity, and the significant drop of the surface rotational velocity for intermediate-mass ( $\gtrsim 1.5M_{\odot}$ ) stars (Gray 1989). At the same time, the photospheres cools down, i.e. the star moves to later spectral types.

As already noted in previous works (e.g. Stepien 1994), this situation is entirely different from the case of main-sequence stars, whose spectral type and internal structure are determined by the stellar mass rather than by the age, and the rotation rate decreases significantly only for low-mass ( $\lesssim 1.5M_{\odot}$ ) stars, due to the torque exerted by magnetically-coupled stellar winds. As a consequence, X-ray emission of late-type dwarfs scales nicely with rotation rate (Pallavicini et al. 1981) or age, and only mildly with the stellar mass (through the properties of the convection zone). We will see shortly that this is not the case for stars in post-main-sequence evolutionary phases.

The behavior of late-type giants and supergiants has been investigated several times in the past, using selected samples of stars observed in X-rays with *Einstein* (Ayres et al. 1981; Maggio et al. 1990), EXOSAT (Gondoin et al. 1987), and ROSAT (Ayres et al. 1995; Hünsch et al. 1996; Reimers et al. 1996; Schröder et al. 1998, Gondoin 1999). Most of these works payed a special attention to characterize the so-called coronal “dividing line” (Ayres et al. 1981), a locus in the H-R diagram, close to the base of the red giant branch, which separates X-

ray luminous yellow giants from K and M giants having very low, if any, magnetic activity. The current picture indicates that intermediate-mass (2–3  $M_{\odot}$ ) G giants in the Hertzsprung gap may reach high X-ray emission levels ( $10^2$ – $10^3$  times higher than a solar-like G dwarf; Maggio et al. 1990), while lower-mass ( $\lesssim 1.5M_{\odot}$ ) evolved stars show weak signs of magnetic activity while in shell-hydrogen burning phases, and they eventually fade out upon reaching the “coronal graveyard” as red giants (Ayres et al. 1991), for reasons not yet completely clear (Rosner et al. 1995; Ayres et al. 1997). As a whole, evolved stars do not follow the activity-rotation relationship so well established for late-type dwarfs (Maggio et al. 1990; Gondoin 1999); on the other hand, their coronal activity appears mass-dependent, although less than expected from theoretical models of convective zone evolution (Gunn et al. 1998), in the framework of a solar-type magnetic dynamo.

A detailed investigation on the X-ray emission level for stars of different mass and age, in early post-main-sequence evolutionary phases, has not been performed yet for several reasons: the limited number of stars in the Hertzsprung gap, due to the short time scale required to cross this region of the H-R diagram; the difficulty to determine with some confidence the stellar mass and to establish the evolutionary phase, because of the uncertainties on distances and absolute magnitudes before the astrometric *Hipparcos* mission; and finally, for the sensitivity limit of previous X-ray surveys.

In order to improve our understanding of the behavior of magnetic activity in stars of different mass, while their internal structure changes rapidly, we have studied the evolution of the coronal X-ray emission and plasma temperature for a sample of stars observed with ROSAT, covering the evolutionary phases from the upper main-sequence to the base of the red giant branch. The novelty of our approach rests on the selection of a sample larger than in previous studies, paying special attention to stars in the Hertzsprung gap rather than to more evolved stars, and on the idea to monitor the variation of the coronal activity with age by considering stars of different spectral types but in restricted mass ranges.

The paper is structured as follows: in Sect. 2 we describe the selection criteria adopted for obtaining our star sample, and in Sect. 3 the methods used to estimate the mass and to compute X-ray luminosities; the results are presented in Sect. 4 and discussed in Sect. 5, where we also draw our conclusions.

## 2. Sample selection and properties

The star sample we have analyzed was obtained by applying several selection steps. The stars were initially extracted from the Bright Star Catalogue (Hoffleit & Warren 1991) in the region of the H-R diagram with  $0 < (B-V) < 1$  and  $-5 < M_v < +5$ . The next step was the availability of ROSAT-PSPC pointed observations. These observations allow to reach a sensitivity limit about two orders of magnitude better than observations in the ROSAT All Sky Survey (RASS) (see Sect. 3). Moreover, we have selected only stars within  $40'$  from the field center (either pointed or serendipitous observations), to avoid observations

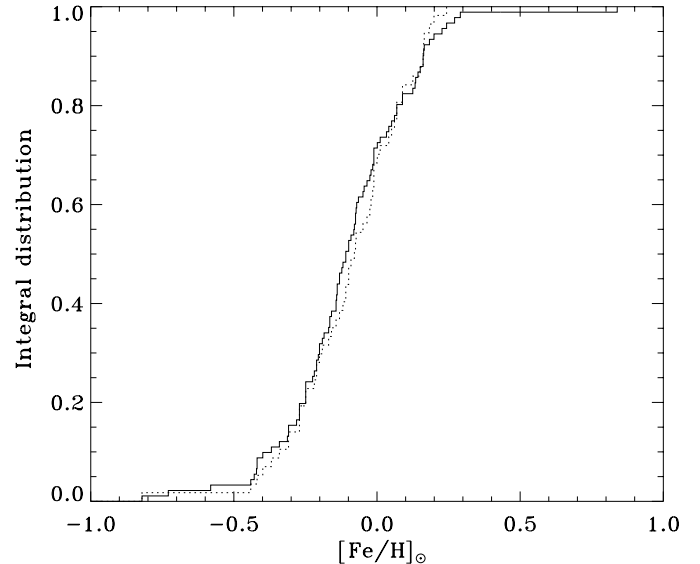


**Fig. 1.** Distributions of  $[Fe/H]_{\odot}$  for  $\sim 43\%$  of the selected sample including main sequence stars (solid line), and for  $\sim 47\%$  of the final sample of evolved stars only (dotted line).

affected by strong vignetting effects, and sources with too large apparent sizes, due to the increasing width of the Point Spread Function (PSF) with increasing off-axis distance. The sample at this stage comprised 219 stars in 316 ROSAT fields.

The selection of the stars in post-main-sequence evolutionary phases was made by using the evolutionary tracks of Schaller et al. (1992; see Sect. 2.1 for more details), transposed from theoretical  $L_{bol} - T_{eff}$  to observational C-M diagram using the transformations of Flower (1996). The most appropriate set of tracks was selected taking into account the metallicity; to this aim, we have investigated the distribution of  $[Fe/H]_{\odot}$  for the fraction ( $\sim 43\%$  of the total) of the selected stars for which metallicity was available from literature (Brown et al. 1989, McWilliam 1990, Cayrel De Strobel et al. 1992, Taylor 1994, Luck & Challener 1995). In Fig. 1 we can see that the  $[Fe/H]_{\odot}$  distribution is centered around the solar value, with 90% of data in the range  $[-0.4, +0.2]$ . We have also tried to match the positions in the H-R diagram of main sequence stars and clump giants with those predicted for them by models assuming different metallicities. Both methods suggest that the tracks with solar metallicity are the most adequate for the selection of evolved stars, in line with the findings by Gondoin (1999). In Fig. 2 we show the H-R diagram with the adopted evolutionary tracks and the locus of the points near the end of the main-sequence phase (exhaustion of core hydrogen); we have then selected only the stars on the right of this locus. For ease of comparison, in Fig. 2 we also show the locus which would have been obtained assuming evolutionary tracks with  $[Fe/H]_{\odot} = 0.2$ . Our sample still includes few class-V star among those with  $B-V < 0.3$  (as for example the F0V star HD 28052, Hyades member): their position in the H-R diagram suggests that these stars may be in the final core-hydrogen burning phases, but – in case of metal-

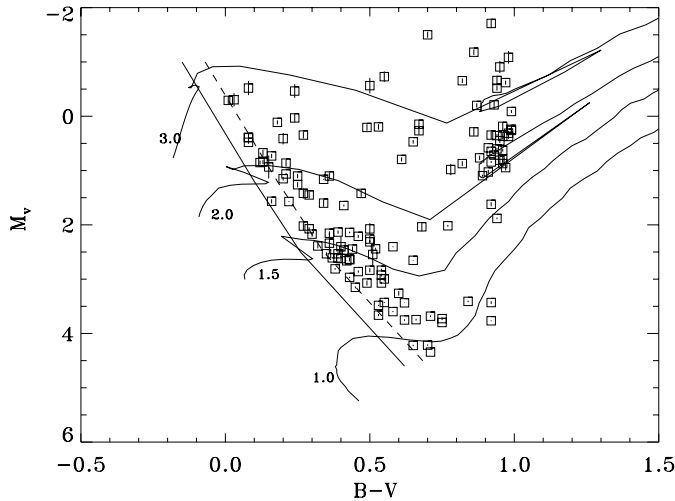


**Fig. 2.** H-R diagram of the evolved stars with Schaller et al. (1992) evolutionary tracks for 1.0 to 3.0 solar masses; the meaning of the solid and the dashed line is explained in the text.

licities higher than solar – an earlier evolutionary stage could be inferred.

We have eventually checked the metallicity distribution of the sample of evolved stars selected at this stage: the general agreement (Fig. 1) with the distribution obtained for the sample including the main-sequence stars, confirms the adequacy of the set of tracks we have chosen. A further control on the evolutionary state of the stars was made using the evolutionary models of Vandenberg (1985; Sect. 2.1): nearly the same star sample would have been selected starting from the latter alternative set of tracks. The 143 stars in the final sample fall in 175 ROSAT-PPSPC fields, with 36 of them observed more than once.

### 2.1. Determination of mass

In order to estimate masses and to check the evolutionary states of the stars in our sample we have used and compared results based on two different sets of evolutionary tracks: (a) the Vandenberg (1985) evolutionary tracks, which assume  $Y = 0.25$  and  $Z = 0.0169$ , and use the mixing length theory of convection with  $\alpha = 1.6$  and no overshooting, Los Alamos opacities (Huebner et al. 1977), and model atmospheres of Kurucz (1979) for the boundary conditions and for transposing the theoretical  $T_{\text{eff}}-L$  diagram into a C-M diagram; (b) the more recent Schaller et al. (1992) evolutionary tracks, with  $Y = 0.3$  and  $Z = 0.020$ , mixing length parameter  $\alpha = 1.6$ , overshooting with  $d_{\text{over}}/H_p = 0.2$  for stars with  $M > 1.25$ , Rogers & Iglesias (1992) opacities and Kurucz (1991) opacities at low temperatures, and updated nuclear reaction rates and neutrino loss rates.

The observational C-M diagram for our sample was based on *Hipparcos* parallaxes, and the stellar masses were computed via interpolation on the tracks, assuming all stars being in the first-crossing evolutionary phases. We have obtained consistent mass estimates, within 10%, using the two sets of tracks (Fig. 3), and we have eventually adopted the masses based on the Schaller

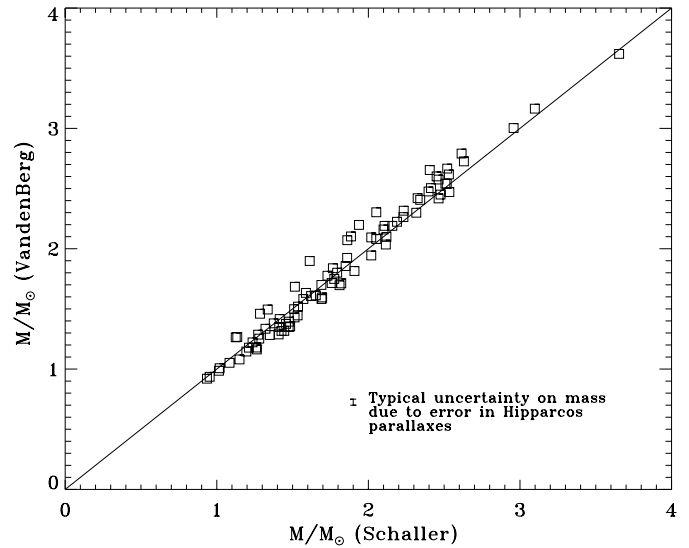


**Fig. 3.** Comparison of masses estimated by interpolating the Vandenberg (1985) evolutionary tracks vs. those obtained from the adopted Schaller et al. (1992) tracks.

et al. evolutionary tracks for our study. As we can see from inspection of Fig. 3, the error on the mass due to the uncertainty on the *Hipparcos* parallax (typically 1%) is smaller than the indetermination on the mass caused by the use of one or the other set of evolutionary tracks, so that the latter source of uncertainty is actually the dominant one. However, this indetermination has little impact on our work because we have eventually selected only four mass ranges for our study.

We have initially chosen  $1.5M_{\odot}$  as a boundary value to separate stars with A-type (or earlier) progenitors on the main-sequence, from late-type stars. This selection is relevant for our investigation because early and late-type stars are expected to show different evolutionary histories of their magnetic activity, because of the differences in convection properties. Each of these two subsamples was further split in two, in order to study the gradual change of the stellar activity evolution for stars with masses increasing from  $\sim 1M_{\odot}$  to  $\sim 3M_{\odot}$ . Note that our sample includes five stars with estimated masses  $< 1M_{\odot}$  (HD 22468, HD 23249, HD 128620, HD 133640, HD 160691) which cannot be considered as evolved stars; while we have not taken them into account for the investigation on the coronal activity evolution, nonetheless we have kept them in the studied sample for comparison purposes.

Finally, note that the stars with  $B-V > 0.8$  and  $M \gtrsim 2M_{\odot}$  suffer of the additional source of uncertainty due to the difficulty of establishing whether they are true first-crossing giants or rather clump giants.

### 2.2. Determination of X-ray luminosity

The ROSAT data were reprocessed with the Palermo-CfA pipeline (Mackie et al. 1996), where source detection and count rate (or upper limit) evaluation are performed with the wavelet transform algorithm of Damiani et al. (1997). The best way

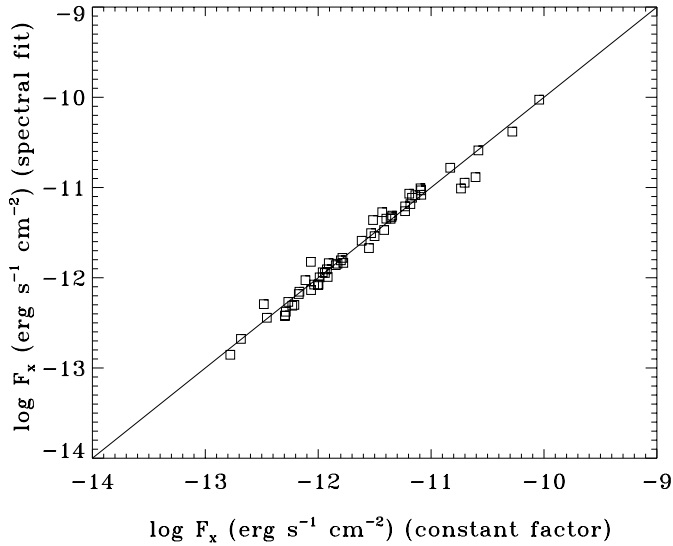


**Fig. 4.** X-ray fluxes computed from spectral fits vs. fluxes estimated using count rates and the median of the count rate-to-flux conversion factors obtained from the spectral fitting results.

to determine X-ray fluxes from count rates, corrected for vignetting effects and background contamination, is that of generating the spectrum of the source and fitting it with a thermal emission model. Then, fluxes can be evaluated from the best-fit model. To this aim, we have fitted spectra with more than 200 total counts, so to get robust fitting results and to reduce the error on the computed flux. One- or two-component isothermal models have been used for the fit, including an interstellar absorption term with the hydrogen column density fixed to the value  $N_{\text{H}} = n_{\text{H}}D$ , where  $n_{\text{H}} = 0.07 \text{ cm}^{-3}$  is the average number density of H atoms in the solar neighborhood ( $D < 100 \text{ pc}$ ; Paresce 1984), and  $D$  is the star distance. The  $\chi^2$  statistics was used to test the goodness of our fitting results, as reported in Table 1. The search of the best-fit parameters and the 90% confidence limits on the fitted temperatures, for each model component, were searched within a grid of 55 thermal spectra, computed at constant steps  $\Delta \log T = 0.05$  over the range  $10^{5.5} - 10^{8.2} \text{ K}$ .

Unfortunately, only 56 observations of the selected stars satisfy the previous condition on the total counts. For the other stars we have adopted a count rate-to-flux conversion factor estimated from the available fitting results. Since the distribution of conversion factors shows a small scatter ( $\sim 3\%$ , Fig. 4), we have used the median value  $1.02 \times 10^{-11} \text{ erg cm}^{-2} \text{ s}^{-1}$  per count  $\text{s}^{-1}$  to evaluate X-ray fluxes for the stars for which spectral fits have not been performed, including those for which only an upper limit on the count rate is available.

We have then studied the variations of the X-ray fluxes measured in multiple ROSAT observations of the same star at different times, searching for possible large flares. In Fig. 5 we show the distribution of the ratios between measured fluxes and the corresponding minimum value for each star: the median of these ratios is  $\sim 1.45$ , 85% of the stars vary less than a factor two, only five stars vary more than a factor two, and none more

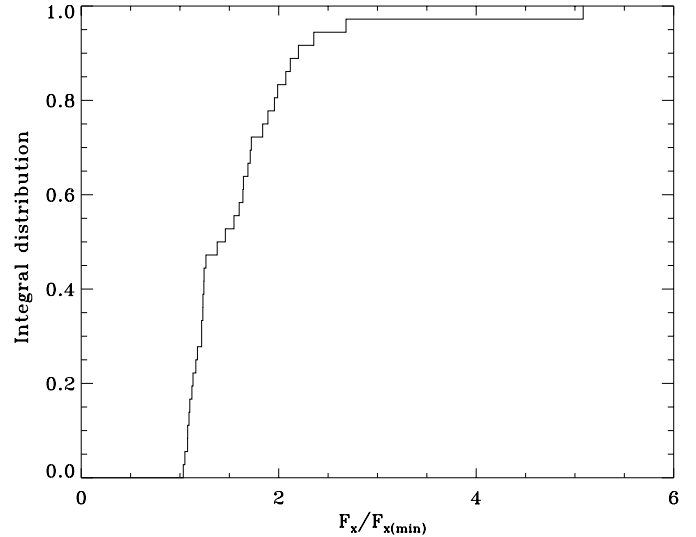


**Fig. 5.** Integral distribution of the ratios  $f_x/\min(f_x)$  for the multiple detections in the ROSAT observations.

than a factor five. This result excludes the occurrence of very large flares. After this check we have calculated the average of the fluxes measured for each star observed more than ones; this value has been used in the rest of this study.

The X-ray fluxes so evaluated have been used to compute X-ray luminosities,  $L_x$ , or upper limits for the non-detected stars, and surface X-ray fluxes by means of stellar radii estimated with the Barnes-Evans relation (Barnes et al. 1978) involving the B-V color. The  $1\sigma$  errors on these parameters take into account the statistical uncertainties on the count rates and the (minor) uncertainties on the parallaxes (on  $L_x$  only).

Fig. 6 shows the distribution of X-ray luminosities,  $L_x$ , vs. stellar distance: the sample adopted so far, being limited in visual magnitude and in X-ray flux, shows an increasing number of stars and a trend of increasing  $L_x$  for increasing stellar distance. In order to obtain a pseudo-volume-limited sample of stars, we have decided to retain for our following analysis only stars with distance  $D < 100 \text{ pc}$ . Our final distance-limited sample contains 120 evolved stars within 100 pc, and from inspection of Fig. 6, we can see that it is nearly free of distance-related observational biases.

In order to check for other possible observational biases due to the sample selection, we have also studied the dependence of X-ray luminosity vs. stellar mass (Fig. 7). There is a tendency for the higher mass stars to be more X-ray luminous, but there exist also high luminosity sources ( $L_x > 29.5 \text{ erg s}^{-1}$ ) with relatively low masses ( $M \leq 2M_{\odot}$ ). This characteristic makes us confident that any residual selection effect is small.

For the stars in the final distance-limited sample we have also collected values of the projected rotational velocity,  $v \sin i$ , available for 100 objects in literature (see Table 2 for references). In particular, we have given preference to the most recent determinations by De Medeiros & Major (1995, 1999) and De Medeiros et al. (1997), obtained from CORAVEL data. All

**Table 1.** One- or Two-temperature model fitting<sup>a</sup> of ROSAT/PSPC spectra.

HD	Obs ID	Total Counts	PI [b]	$\log N_{\text{H}}$ $\text{cm}^{-2}$	$T_1$ $10^6$ K	$EM_1$ [c]	$T_2$ $10^6$ K	$\frac{EM_2}{EM_1}$	$f_{\text{x1}}$ [d]	$f_{\text{x2}}$ [d]	$\chi^2_{\text{r}}/\text{dof}$
432	201520	560	21	18.5	1.4 (1.0, 1.8)	17	7.9 (4.0,11.2)	0.5	9	7	0.6/13
6793	200975	530	26	19.5	4.0 (2.0, 6.3)	1114	14.1 (> 10.0)	3.6	31	62	0.6/18
10308	200539	573	26	19.0	1.8 (0.9, 2.5)	331	10.0 (7.1,17.8)	1.7	18	35	0.7/18
16555	300201	212	21	19.0	2.2 (2.2, 2.5)	16			1		0.9/15
17824	201543	444	23	19.0	4.0 (4.0, 4.5)	197			13		0.4/17
20675	201510	856	26	19.0	1.6 (1.1, 2.0)	17	6.3 (5.0, 7.9)	1.1	1	2	0.8/18
22468	200844	30391	34	19.0	3.5 (3.5, 4.5)	1073	15.8 (15.8,22.4)	5.2	252	680	10.4/26
27371	200775	1400	26	19.0	4.5 (4.5, 4.5)	295			29		1.4/20
27697	200442	189	23	19.0	2.5 (2.2, 2.8)	22			2		1.2/17
27991	200777	3034	28	19.0	1.6 (1.4, 2.0)	67	7.1 (6.3, 7.9)	1.1	5	10	0.4/20
28052	200777	9671	32	19.0	2.2 (2.0, 2.2)	474	11.2 (10.0,11.2)	1.8	39	59	1.6/24
28307	200778	1015	25	19.0	1.6 (1.3, 2.0)	289	7.1 (6.3, 7.9)	1.8	20	62	1.2/17
35317	200927	212	21	19.0	2.0 (1.8, 2.2)	137			7		0.8/15
35317	200927a1	264	21	19.0	2.2 (2.0, 2.2)	182			10		1.0/15
36079	200174	562	23	19.0	1.6 (1.1, 2.0)	32	7.1 (4.0,10.0)	0.5	2	2	0.7/15
41116	201225	621	23	19.0	1.6 (1.0, 2.2)	20	5.6 (4.0, 7.9)	1.4	2	3	0.7/15
45348	200319	1379	28	19.5	3.5 (2.0, 4.5)	948	11.2 (8.9,17.8)	1.5	20	24	0.4/20
48737	201487	548	24	18.5	1.8 (0.6, 4.0)	10	7.9 (5.6,14.1)	2.7	6	23	0.7/16
50241	200638	682	25	19.0	1.6 (1.4, 2.0)	12	7.9 (6.3,10.0)	0.8	2	3	0.9/17
61421	200437	9265	21	18.0	1.3 (1.3, 1.4)	8	4.0 (3.2,11.2)	0.1	105	8	2.6/13
61421	201118	4886	23	18.0	1.4 (1.4, 1.4)	7	7.9 (> 3.5)		94	4	1.1/15
71243	201489	672	23	18.5	3.5 (1.4, 4.0)	25	22.4 (> 4.5)	0.5	13	3	2.0/15
82210	200318	1562	31	19.0	2.2 (1.4, 2.8)	263	10.0 (8.9,11.2)	2.4	48	118	1.0/23
86146	700526	521	22	19.0	1.4 (1.1, 1.6)	21	7.9 (5.0,11.2)	0.4	4	3	0.5/14
89449	200076	1757	28	18.5	1.6 (1.4, 2.0)	24	6.3 (5.6, 7.9)	1.2	9	17	1.2/20
102870	200813	2283	25	18.5	1.6 (1.4, 1.8)	9	5.6 (4.5, 7.1)	0.5	12	10	1.4/17
107700	201167	575	27	19.5	2.0 (0.6, 4.0)	494	8.9 (> 7.1)	2.1	13	34	0.7/19
111812	200973	994	30	19.5	11.2 (10.0,11.2)	4478			79		1.3/24
119756	800287	2851	28	18.5	2.0 (1.6, 2.2)	61	7.1 (6.3, 7.9)	1.2	30	55	1.0/20
121370	700804	746	24	18.5	2.2 (2.2, 2.2)	11			16		1.3/18
124850	200908	2072	32	18.5	1.8 (1.4, 2.5)	26	7.9 (7.9, 8.9)	3.1	10	45	0.9/24
128620	201119	7695	26	17.5	1.3 (1.3, 1.3)	1	5.0 (4.0, 5.6)	0.1	107	23	1.6/18
128620	180025	2153	33	17.5	1.6 (1.6, 1.8)	2	8.9 (7.9,10.0)	0.7	208	209	1.2/25
129926	200134a1	288	22	19.0	2.5 (2.5, 2.8)	51			11		0.7/16
131041	900584	230	23	19.0	8.5 (> 3.5)	605			7		0.5/17
133208	201536	712	29	19.0	2.2 (1.8, 3.5)	48	11.2 (8.9, 89.1)	1.9	2	3	0.7/21
133640	200841	6803	34	18.5	2.2 (2.0, 2.5)	99	8.9 (8.9,10.0)	1.0	116	142	2.8/26
136351	200464	186	23	19.0	3.5 (3.2, 4.0)	46			8		0.6/17
148856	201228	555	24	19.0	3.5 (3.5, 4.0)	89			9		1.1/18
150997	201538	664	25	19.0	4.0 (4.0, 4.0)	56			10		1.2/19
155203	200132	195	17	18.5	2.0 (1.8, 2.2)	20			8		0.4/11
157950	400389	904	25	19.0	1.8 (1.4, 2.2)	19	7.9 (6.3, 8.9)	1.4	4	8	0.8/17
160922	999995	2634	27	18.5	1.6 (1.6, 1.8)	69	7.9 (7.1, 8.9)	0.9	20	29	0.8/19
160922	999995a1	1370	25	18.5	1.6 (1.4, 2.0)	61	5.6 (4.5, 7.9)	1.0	18	27	0.6/17
163993	200972	832	31	19.0	5.0 (4.5, 5.0)	601			82		0.9/25
166865	999999a3	219	21	19.0	2.8 (> 2.5)	55			4		0.8/15
171391	500126	1504	29	19.5	1.6 (0.9, 4.0)	147	7.9 (7.9, 8.9)	8.3	3	41	1.2/21
175225	200976	1325	31	19.0	2.5 (2.0, 3.2)	93	11.2 (10.0,15.8)	1.8	26	39	1.0/23
175813	200493	806	26	19.0	1.4 (1.1, 2.0)	34	5.6 (4.0, 7.9)	0.9	6	9	0.8/18
175813	900002	686	23	19.0	1.8 (1.3, 2.2)	32	7.1 (4.0,10.0)	0.5	6	5	1.1/15
181391	400274	1410	27	19.0	2.2 (1.8, 2.8)	54	8.9 (6.3,12.6)	0.8	5	5	1.0/19
181391	200550	190	24	19.0	4.0 (3.5, 5.0)	119			11		0.5/18
205435	200974	949	26	19.0	1.6 (1.0, 2.5)	56	6.3 (5.0, 7.9)	2.7	6	28	0.6/18
211391	201539	482	22	19.0	4.5 (4.0, 4.5)	132			8		0.8/16
220657	200322	16432	34	19.0	1.6 (1.6, 1.8)	112	8.9 (8.9, 8.9)	6.0	6	55	3.3/26

<sup>a</sup> The 90% joint confidence ranges on  $T_1$  and  $T_2$  have been computed with the criterium  $\chi^2 < \chi^2_{\text{min}} + 4.61$ .

Hydrogen column density was kept fixed to a value estimated from the star distance.

<sup>b</sup> Last PSPC channel used for the the spectral fitting.<sup>c</sup> Plasma emission measure, in units of  $10^{50} \text{ cm}^{-3}$ <sup>d</sup> X-ray fluxes in units of  $10^{-13} \text{ erg cm}^{-2} \text{ s}^{-1}$ , at the source, in the 0.2–4 keV band.

**Table 2.** Data of the distance-limited star sample.

HD	S/B <sup>1</sup>	Parallax mas	B-V	$M_V$	Mass $M_{\odot}$	$L_x$ $10^{28} \text{ erg s}^{-1}$	$\log F_x$ $\text{erg/cm}^2 \text{ s}^{-1}$	$\log f_x/f_{\text{bol}}$	$v \sin i$ $\text{km s}^{-1}$	$P_{\text{rot}}$ days
432	B	59.89	0.34	1.16	1.97	5.5	4.9	-6.3	70.0 b	0.1 d
2151	S	133.78	0.62	3.44	1.27	0.3	4.1	-6.7	6.0 a	
2885	B	18.95	0.15	0.93	1.99	5.9	5.1	-6.3	50.0 b	
5015	B	53.85	0.53	3.48	1.20	1.8	5.1	-5.8	6.0 b	128.0 d
6793	S	11.68	0.88	0.77	2.31	817.6	6.2	-4.4		
10308	B	17.86	0.44	2.45	1.51	200.0	6.8	-4.2	12.0 b	4.4 d
10697	S	30.71	0.75	3.73	1.15	1.6	4.8	-5.8	1.3 a	
16417	S	39.16	0.66	3.75	1.16	< 0.6	< 4.5	< -6.2		
16555	S	22.49	0.27	2.02	1.59	3.5	5.1	-6.1	239.0 b	
17824	B	17.85	0.91	1.03	2.03	48.5	5.0	-5.5		
18925	B	12.72	0.70	-1.50	4.34	< 2.3	< 2.9	< -7.8	50.0 b	5350.0 d
20675	S	21.86	0.43	2.64	1.43	9.0	5.6	-5.5		
22468	B	34.52	0.92	3.43	0.90	935.9	7.2	-3.2	14.8 a	2.8 e
22484	S	72.89	0.58	3.60	1.18	0.2	4.0	-6.9	2.4 b	
23249	S	110.58	0.92	3.77	0.84	0.2	3.6	-6.9	1.0 a	
26015	B	21.27	0.40	2.62	1.42	12.8	5.7	-5.3	25.0 b	
27371	B	21.17	0.99	0.26	2.40	77.2	4.8	-5.6	1.0 a	
27697	B	21.29	0.98	0.37	2.33	5.0	3.7	-6.8	1.2 a	529.8 d
27991	B	21.47	0.49	3.07	1.32	37.9	6.3	-4.7	15.0 b	
28052	B	20.86	0.25	1.10	1.94	269.5	6.7	-4.6	192.0 b	5200.0 d
28307	B	20.66	0.95	0.45	2.35	230.7	5.4	-5.1	1.5 a	3000.0 d
28319	B	21.89	0.18	0.11	2.42	3.2	4.4	-6.9	78.0 b	140.7 d
28485	B	22.93	0.32	2.39	1.47	11.8	5.7	-5.4	134.0 b	30.5 d
28910	B	21.39	0.25	1.26	1.88	2.1	4.6	-6.6	117.0 b	488.5 d
30478	S	14.66	0.20	1.15	1.91	2.6	4.7	-6.6	177.0 b	
35162	B	11.09	0.67	0.27	2.89	11.7	4.4	-6.3		
35317	B	17.23	0.50	2.26	1.64	35.9	5.9	-5.0		
36079	B	20.49	0.82	-0.66	3.61	12.0	3.9	-6.7	5.2 a	
36584	B	13.16	0.34	1.60	1.78	< 22.0	< 5.7	< -5.5		
37495	S	23.54	0.46	2.21	1.62	26.9	5.8	-5.2	31.0 b	
39014	S	22.48	0.21	1.06	1.95	1.6	4.5	-6.8	206.0 b	
40932	B	21.49	0.16	0.73	2.08	21.8	5.5	-5.8	24.0 b	4.4 d
41116	B	21.64	0.82	0.87	2.39	12.5	4.5	-6.1	1.7 a	9.6 d
45348	S	10.43	0.15	-5.72	> 5.00	491.7	4.3	-7.1		
45588	B	33.48	0.53	3.66	1.13	0.8	4.8	-6.1		
48737	S	57.02	0.43	2.14	1.62	10.6	5.4	-5.6	70.0 b	
50241	S	32.96	0.21	0.86	2.04	5.5	4.9	-6.4	205.0 b	
55864	B	22.16	0.40	2.40	1.50	8.3	5.5	-5.6		
58728	B	29.38	0.39	2.53	1.45	70.4	6.5	-4.6	38.0 b	1.9 d
61421	S	285.93	0.42	2.66	1.42	1.5	4.8	-6.2	6.1 a	14837.3 d
71243	S	51.40	0.39	2.61	1.42	7.2	5.5	-5.6	28.6 a	
74772	B	14.27	0.87	-0.20	3.13	27.6	4.3	-6.2	5.8 a	
77258	B	16.19	0.65	0.47	2.74	152.5	5.6	-5.1	15.0 b	74.1 d
80499	B	10.20	0.93	-0.21	3.02	< 7.8	< 3.7	< -6.8	10.0 c	
82210	S	30.89	0.77	2.02	1.81	207.4	6.2	-4.4	5.5 a	
84737	S	54.26	0.62	3.75	1.14	< 0.3	< 4.2	< -6.6	3.0 b	
86146	B	34.61	0.46	2.86	1.38	6.6	5.5	-5.5	3.0 c	9.3 d
89449	S	47.24	0.45	3.15	1.27	13.8	5.9	-5.1	17.3 a	
89744	S	25.65	0.54	2.83	1.45	< 4.3	< 5.2	< -5.7	8.0 b	
94601	B	11.29	0.01	-0.29	2.59	< 10.7	< 5.0	< -6.6	182.0 b	
101606	S	24.42	0.43	2.63	1.44	< 1.9	< 4.9	< -6.1	5.0 c	
102590	B	13.48	0.29	1.45	1.81	8.1	5.2	-6.0		
102870	S	91.74	0.55	3.43	1.23	3.0	5.2	-5.6	3.0 b	
107213	S	20.12	0.50	2.83	1.42	< 1.8	< 4.8	< -6.1	8.0 b	
107326	S	16.50	0.30	2.17	1.54	4.9	5.3	-5.9	109.0 b	
107398	B	10.83	0.36	2.34	1.50	24.8	6.0	-5.1		
107700	B	11.93	0.49	0.21	2.65	393.5	6.2	-4.8	3.9 a	396.5 d
107966	S	11.47	0.08	0.39	2.24	13.9	5.3	-6.2	54.0 b	
108007	B	10.23	0.27	1.42	1.81	9.1	5.3	-5.9	148.0 b	
108283	B	11.92	0.27	0.35	2.34	< 6.3	< 4.7	< -6.5	226.0 c	
108382	S	11.56	0.08	0.40	2.24	< 5.0	< 4.9	< -6.6	89.0 b	
111812	S	10.62	0.67	0.15	2.96	841.4	6.2	-4.5	66.5 a	
113226	S	31.90	0.94	0.36	2.47	4.2	3.6	-6.8	2.3 a	

**Table 2.** (continued)

HD	S/B <sup>1</sup>	Parallax mas	B-V	$M_v$	Mass $M_{\odot}$	$L_x$ $10^{28} \text{ erg s}^{-1}$	$\log F_x$ $\text{erg/cm}^2 \text{ s}^{-1}$	$\log f_x/f_{\text{bol}}$	$v \sin i$ $\text{km s}^{-1}$	$P_{\text{rot}}$ days
117176	S	55.22	0.71	3.68	1.19	< 0.2	< 3.9	< -6.9	1.0 b	
118232	S	17.12	0.12	0.85	2.02	< 6.7	< 5.1	< -6.3	178.0 b	
119756	B	51.91	0.38	2.81	1.35	37.9	6.3	-4.8	86.0 b	9.9 d
121370	B	88.17	0.58	2.40	1.67	2.5	4.7	-6.1	13.0 a	494.2 d
124553	S	24.09	0.60	3.26	1.33	8.5	5.6	-5.3	8.0 d	
124570	B	30.06	0.54	2.93	1.42	< 2.8	< 5.0	< -5.9	5.6 a	726.6 d
124850	S	46.74	0.52	2.44	1.59	30.0	5.9	-5.0	14.8 a	
125337	B	17.47	0.13	0.67	2.11	< 1.0	< 4.2	< -7.2	16.0 b	1.9 d
128620	B	742.12	0.71	4.34	0.94	0.6	4.7	-6.0	2.7 c	29630.7 d
129422	B	21.75	0.29	2.07	1.57	< 2.5	< 5.0	< -6.2	213.0 b	
129926	B	32.86	0.35	2.53	1.43	11.6	5.7	-5.4	161.0 b	
131041	B	14.22	0.47	1.42	1.98	41.4	5.7	-5.3		12.8 d
133208	S	14.91	0.97	-0.62	3.35	29.1	4.0	-6.4	2.5 a	
133640	B	78.39	0.65	4.22	0.97	50.2	6.6	-4.1	16.0 b	0.3 d
134505	S	28.06	0.92	0.65	2.29	< 0.3	< 2.6	< -7.9		
136202	B	40.46	0.54	3.07	1.36	0.6	4.4	-6.5	4.8 a	
136351	S	29.27	0.50	2.31	1.62	10.9	5.4	-5.5	50.0 b	
138852	S	10.24	0.96	0.79	2.05	< 9.9	< 4.2	< -6.3	1.2 a	
139521	S	13.32	0.99	0.24	2.42	< 4.8	< 3.6	< -6.8		
146791	S	30.34	0.96	0.63	2.18	< 0.3	< 2.5	< -8.0	< 17.0 b	
148048	S	33.52	0.37	2.61	1.41	11.5	5.7	-5.4	76.0 b	
148387	B	37.18	0.91	0.58	2.37	1.6	3.4	-7.2	1.2 a	
148856	B	22.07	0.94	-0.52	3.32	20.9	4.0	-6.5	4.8 a	410.6 d
148898	S	18.66	0.13	0.84	2.03	15.2	5.5	-6.0	41.0 b	
150680	B	92.63	0.65	2.65	1.61	1.3	4.4	-6.3	4.8 a	12562.2 d
150997	S	29.11	0.92	0.84	2.13	13.7	4.4	-6.1	1.7 a	
154948	B	10.87	0.86	0.29	2.73	30.1	4.6	-6.0		
155203	S	45.56	0.41	1.64	1.81	4.4	4.9	-6.2	150.0 b	
157950	B	33.28	0.39	2.13	1.60	12.2	5.5	-5.5	50.0 c	26.3 d
160691	S	65.46	0.70	4.21	0.98	0.3	4.3	-6.4		
160922	B	42.62	0.43	2.97	1.32	30.9	6.2	-4.8	26.0 b	5.3 d
161797	S	119.05	0.75	3.80	1.12	0.2	3.9	-6.8	1.7 a	
163993	S	24.12	0.94	0.60	2.26	169.5	5.3	-5.1	3.2 a	
165760	S	13.71	0.96	0.37	2.40	< 5.0	< 3.7	< -6.8	2.2 a	
166865	B	19.64	0.51	2.54	1.54	12.7	5.6	-5.4	25.0 b	10.5 d
166866	B	18.84	0.50	2.07	1.72	13.8	5.4	-5.5	13.0 c	
168723	S	52.81	0.94	1.88	1.42	< 0.2	< 3.0	< -7.5	< 19.0 b	
171391	S	11.25	0.92	0.35	2.53	412.3	5.7	-4.8	< 19.0 b	
172088	B	20.01	0.55	3.00	1.40	8.7	5.5	-5.3		
173582	S	20.10	0.16	1.56	1.75	15.4	5.7	-5.7	200.0 b	
175225	B	38.32	0.84	3.41	1.12	53.4	6.1	-4.5	1.0 a	
175813	B	33.43	0.41	2.46	1.49	13.9	5.7	-5.3	132.0 b	0.6 d
181391	B	21.17	0.92	1.62	1.64	27.2	5.0	-5.5	2.8 a	266.5 d
190004	B	15.43	0.36	1.10	2.01	5.7	4.8	-6.3	121.0 b	
199870	B	12.32	0.97	0.95	1.90	13.3	4.3	-6.1	1.2 a	635.1 d
200011	B	12.28	0.68	2.04	1.93	18.3	5.3	-5.4		
202109	B	21.62	0.99	-0.09	2.73	< 0.5	< 2.5	< -8.0	1.0 a	
202447	B	17.51	0.53	0.20	2.72	< 38.7	< 5.1	< -5.8	20.0 a	98.8 d
203280	S	66.84	0.22	1.57	1.74	0.3	4.0	-7.3	246.0 b	
205435	S	26.20	0.89	1.09	2.05	58.9	5.1	-5.4	1.9 a	
206356	B	13.18	0.95	0.81	2.06	< 4.3	< 3.8	< -6.6		
211391	S	17.04	0.98	0.31	2.39	34.2	4.5	-6.0	< 17.0 b	
215182	B	15.18	0.86	-1.18	4.16	< 4.0	< 3.1	< -7.4	1.7 a	818.0 d
215664	S	18.79	0.36	2.15	1.57	< 1.7	< 4.7	< -6.4	170.0 c	
215789	S	25.16	0.08	0.48	2.20	1.6	4.4	-7.1	236.0 b	
216131	S	27.95	0.93	0.72	2.20	0.2	2.4	-8.1	1.2 a	
220657	S	18.83	0.61	0.79	2.52	208.6	6.0	-4.9	33.7 a	

<sup>1</sup> Single/Binary flagReferences for  $v \sin i$  and  $P_{\text{rot}}$ : (a) De Medeiros & Mayor (1995, 1999), De Medeiros et al. (1997); (b) BSC5; (c) Simbad database; (d) Balachandran (1990); (e) Fekel (1997)References for  $P_{\text{rot}}$  (only for spectroscopic binaries): (d) Batten et al. (1989); (e) Strassmeier et al. (1993)

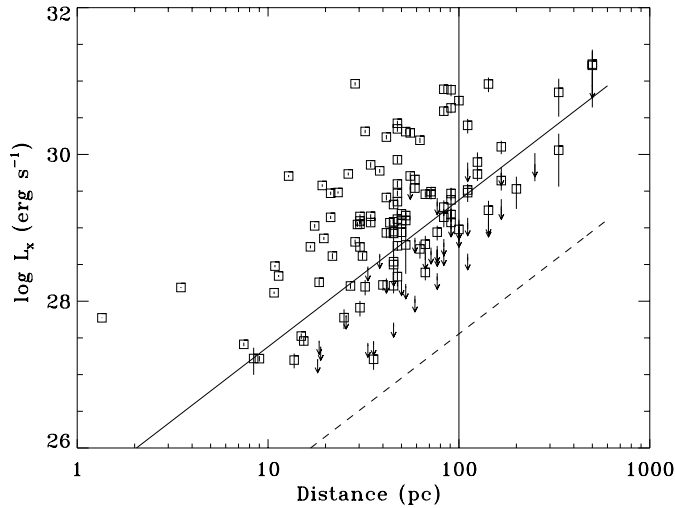


**Fig. 6.** X-ray luminosity vs. stellar distance. The dashed line indicates the sensitivity threshold for ROSAT-PSPC observations,  $f_x \sim 3 \times 10^{-15} \text{ erg s}^{-1} \text{ cm}^{-2}$ , which could be achieved with an exposure time of  $10^4$  s; the parallel solid line shows instead the sensitivity of a typical ROSAT-PSPC observation, corresponding to a flux of  $\sim 3 \times 10^{-13} \text{ erg s}^{-1} \text{ cm}^{-2}$ . The vertical line marks the distance limit of our final sample.

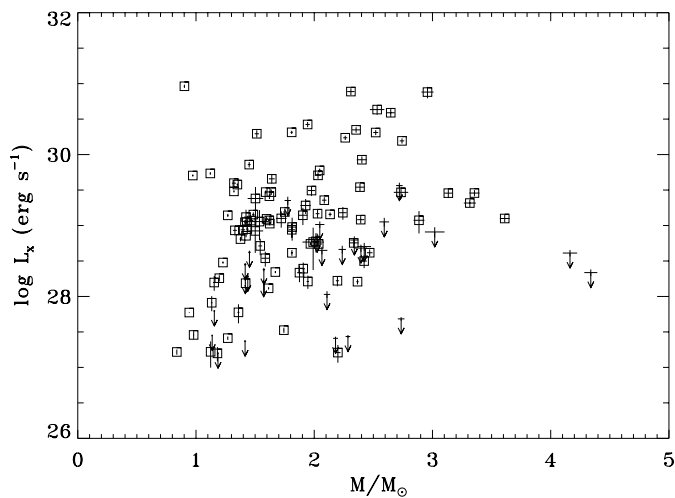


**Fig. 7.** Scatter plot of X-ray luminosity (or upper limit) vs. stellar mass for the stars in the ROSAT sample with  $D < 100$  pc.

the stellar data required for our following analysis are listed in Table 2.

### 3. Results

Our final sample contains 42 single stars and 78 binaries (from SIMBAD database information), 44 of them being spectroscopic binaries (SB). From the observational point of view, a spectroscopic binary star or a multiple stellar system not resolved in X-rays may imply an overestimation of the flux associated to the evolved star under examination. From an interpretative point of view, multiple systems, with stars at a distance such that mass exchange between components or tidal effects

may occur, can be characterized by a dynamo efficiency and level of X-ray emission different with respect to single stars of similar mass. Checking the PSPC images we have resolved 13 binary stars having an angular separation  $\gtrsim 60''$ , according to the Bright Star Catalogue. To further increase the number of resolved stars we have examined also 16 images obtained with the High Resolution Imager (HRI) on board of ROSAT, having a better angular resolution ( $\sim 2.5''$  on the axis) than the PSPC, and a useful field of view of  $\sim 30'$ . One more star was resolved in this way. These 14 stars were studied together with the other 42 single stars, already selected.

#### 3.1. X-ray emission level vs. evolutionary phase

In order to monitor the variation of X-ray activity during the evolution across the Hertzsprung gap, we have studied the distribution of X-ray luminosities vs. B-V color for single and binary stars separately, in each selected mass range (Fig. 8 and 9). In fact, since the evolutionary tracks are almost horizontal in the H-R diagram, during early post-main-sequence phases, the B-V color can be used as a proxy of the evolutionary age. To the aim of looking for trends in the data with a non-parametric statistical approach, we have employed a procedure called LOWESS (for locally-weighted scatterplot smoother; Cleveland 1979), also known as robust locally-weighted regression<sup>1</sup>. The following scenario appears evident:

- $M/M_{\odot} < 1.3$ : most of the stars with  $M > 1M_{\odot}$  (G-type on the main-sequence) show relatively low X-ray emission levels ( $27 < \log L_x < 29.5 \text{ erg s}^{-1}$ ) in the B-V range 0.4–0.9, and there is a tendency of decreasing  $L_x$  vs. B-V. The only three stars with  $\log L_x > 29.5 \text{ erg s}^{-1}$  in this subsample are GJ 732.1 (HD 175225), a suspected spectroscopic binary (Duquennoy & Mayor, 1991), and two of the five stars with  $M < 1M_{\odot}$ , i.e. the well-known W UMa-type short period binary 44 Boo (HD 133640), and the RS CVn-type system HR 1099 (HD 28468). These two latter stars are indeed “peculiar”, however their inclusion does not affect any of our results because they are recognized as outliers by our robust regression. We have no a priori clue on why GJ 732.1 shows such a high X-ray luminosity.
- $1.3 < M/M_{\odot} < 1.5$ : these stars (F and G-type on the main-sequence) appear on average slightly more X-ray luminous ( $28 < \log L_x < 30 \text{ erg s}^{-1}$ ) with respect to lower mass stars with similar color, and there is little if any dependence of  $L_x$  on B-V, up to B-V  $\sim 0.5$ . Beyond B-V = 0.6 the only star in

<sup>1</sup> In short, at each X position in a scatter plot, this procedure computes a smoothed Y value by performing a weighted regression of the data in a sliding window, comprising about 2/3 of the data points (smoothing parameter). The weight of each point is given by the product of two terms, a decreasing function of the distance from the center of the window, and a decreasing function of the residual with respect to the smoothed curve, the latter contribution evaluated iteratively. If upper limits are present in the window (censored data), we take them into account with a third weighting term given by the Kaplan-Meier estimator of the distribution function of the data in the window.



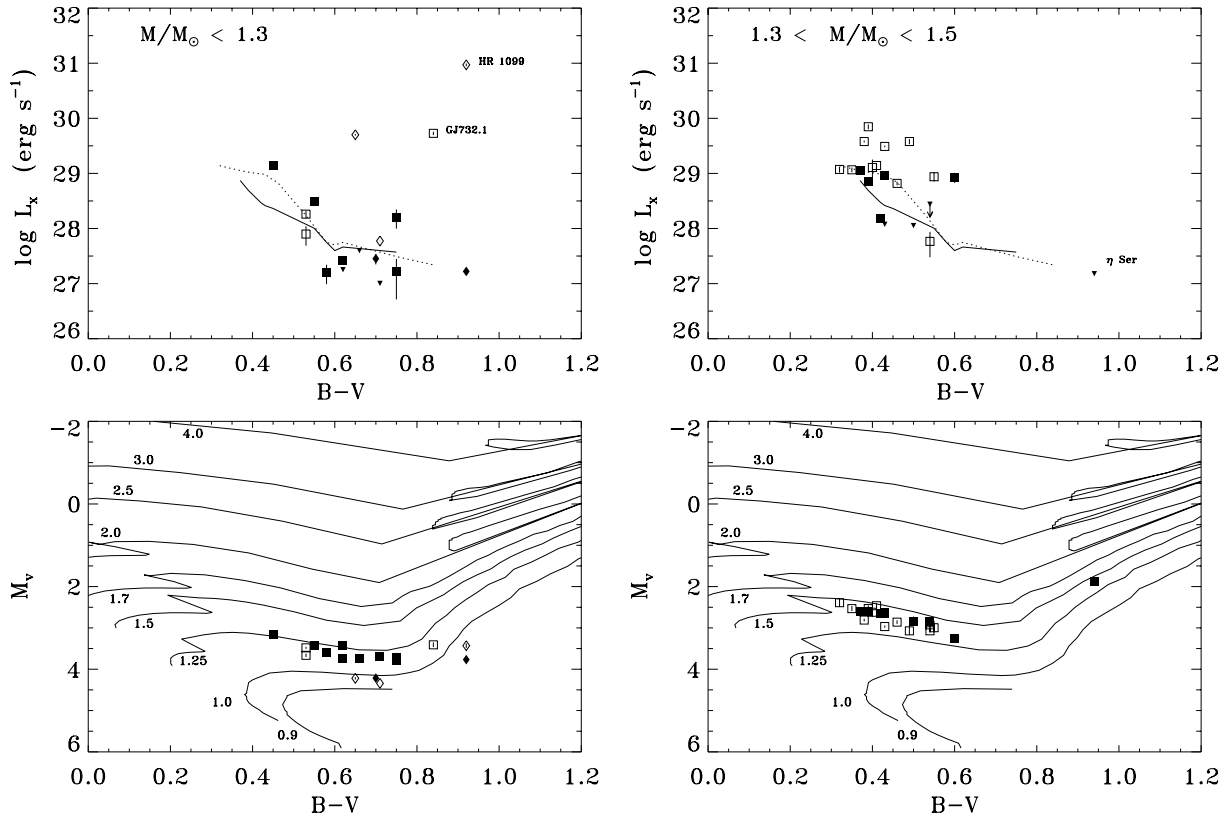


**Fig. 8.** Distributions of X-ray luminosities (or upper limits) vs. B-V color for single and resolved binary stars (filled symbols) and unresolved binaries (open symbols), in the two mass ranges indicated in the upper panels. Five stars with estimated masses  $< 1M_{\odot}$ , indicated with diamonds, are included for comparison purposes only. Note that the errors on X-ray luminosities are often smaller than the symbol size. The lines are the result of a LOWESS regression (see text) applied separately to the subsamples of single (solid line) and binary (dotted line) stars, in the single range of masses  $1 < M/M_{\odot} < 1.5$ . The bottom panels show the corresponding H-R diagrams, including the Schaller et al. (1992) evolutionary tracks.

this mass range is  $\eta$  Ser (HD 168723), showing a low upper limit on its X-ray luminosity ( $L_x < 1.4 \times 10^{27}$  erg s $^{-1}$ ). One more W UMa-type system is present in this subsample (HD 175813, B-V=0.41,  $L_x = 1.4 \times 10^{29}$  erg s $^{-1}$ ), but - unlike the case of 44 Boo - its X-ray emission level is typical of other single and binary stars with similar mass and B-V color.

- $1.5 < M/M_{\odot} < 2.0$ : the single stars in this mass range (A-type on the main sequence) show instead, on average, an increasing X-ray emission level during the evolutionary phases across the Hertzsprung gap, from  $\log L_x \lesssim 28$  erg s $^{-1}$  to  $\gtrsim 30.5$  erg s $^{-1}$ ; the binary stars follow a similar trend up to B-V  $\sim 0.5$ , but all the other stars with redder colors have X-ray luminosities below  $L_x \sim 5 \times 10^{29}$  erg s $^{-1}$ , with the most notable examples (located around B-V  $\approx 0.6$ ) being  $\eta$  Boo (HD 121370), a G0 IV spectroscopic binary with  $v \sin i \sim 13$  km s $^{-1}$ , and 40 Her (HD 150680), a G0 IV spectroscopic binary with  $v \sin i \sim 4.8$  km s $^{-1}$ . There are also two binary stars with X-ray luminosity exceeding  $L_x \sim 10^{30}$  erg s $^{-1}$  and B-V  $< 0.5$ : the spectroscopic binary 71 Tau (HD 28052, F0 V), member of the Hyades cluster, with  $v \sin i \sim 193$  km s $^{-1}$ , and HD 10308, F2 III, member of a triple-system, having  $v \sin i \sim 12$  km s $^{-1}$ . The single

star with the highest X-ray luminosity is the well-known gap giant 24 UMa (HD 82210; Ayres et al. 1998).

- $2.0 < M/M_{\odot} < 3.0$ : these stars show the same increasing trend as the previous subsample. The two X-ray luminous single stars with B-V = 0.6–0.7 are the bona-fide gap giants  $v$  Peg (HD 220657) and 31 Com (HD 111812), while the star with B-V  $> 0.8$  with the highest X-ray luminosity is  $\iota$  Tuc (HD 6793). The only star well below the average path is the binary HD 35162 at B-V  $\approx 0.65$ . Among the stars with B-V  $> 0.8$  we observe a large range of X-ray emission levels ( $27 < \log L_x < 31$  erg s $^{-1}$ ), possibly due to mixing of stars ascending the giant branch for the first time and clump giants (see discussion below).
- $M/M_{\odot} > 3.0$ : only 7 stars in this mass range are included in our sample, including just one single star, and most of them (6 out of 7) have B-V  $> 0.8$ , so we are unable to study in detail their evolutionary history; however, their X-ray luminosities (or upper limits) are comprised in the wide range spanned by the stars in the previous subsample with similar red colors.

Since in these phases the stellar radius increases appreciably, and the X-ray luminosity may depend on the available stellar

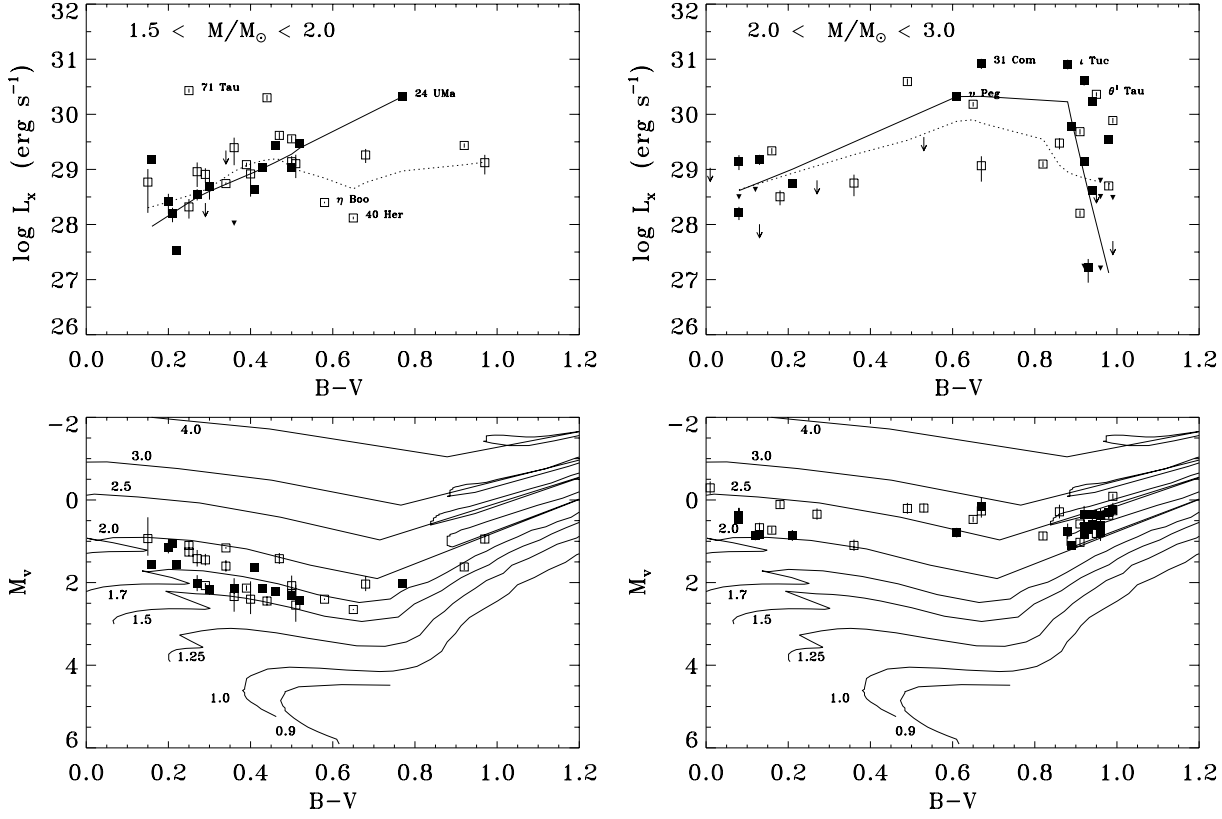


**Fig. 9.** Similar to Fig. 8, but for two different mass ranges. The LOWESS regression has been applied separately to single and binary stars in each indicated mass range.

surface, we have inspected also the distributions of surface X-ray fluxes vs. B-V color (Fig. 10). Even using this parameter, there is a clear decay of the coronal emission for the lower mass stars ( $M < 1.5M_{\odot}$ ), and a trend for increasing emission levels for the intermediate-mass stars, up to B-V  $\sim 0.8$ , followed by a large spread for redder stars.

### 3.2. Coronal temperatures

In Fig. 11 we show our spectral fitting results. Inspection of the scatter plot of  $L_x$  vs. temperature, for the individual thermal components, suggests that two effects occur as the total coronal X-ray luminosity increases: the temperatures of the individual components tend to increase, and at the same time the relative contribution to the X-ray emission of the cooler vs. the hotter component gradually shifts from dominant low-temperature components ( $T_1 \sim 1\text{--}2\text{ MK}$ ) to dominant high-temperature components ( $T_2 \sim 4\text{--}16\text{ MK}$ ). The latter results is confirmed by the scatter plot of the total X-ray luminosity vs. the hot/cool emission measure ratio, shown in Fig. 11b: for  $EM_2/EM_1 > 0.1$ , the trend found with a *lowess* regression can be well approximated with the power law  $L_x \propto (EM_2/EM_1)^{1.6}$ , and the emission measure ratio becomes greater than one (hotter component dominant) for  $L_x \gtrsim 2.5 \times 10^{29} \text{ erg s}^{-1}$ . Finally, we have evaluated average temperatures from the 2-T model fits, weighting the two components with the respective emission measures:

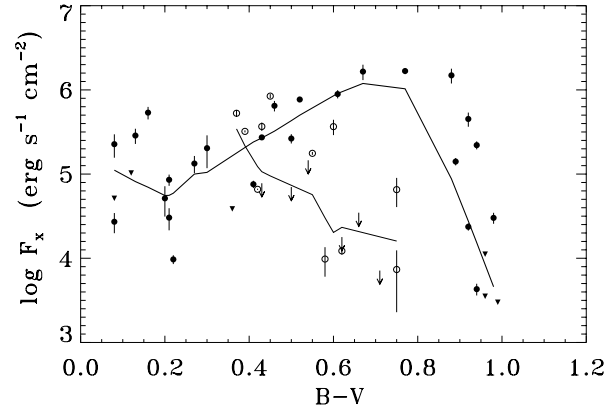


**Fig. 10.** Surface X-ray fluxes vs. B-V color for single stars in the mass ranges  $1 < M/M_{\odot} \leq 1.5$  (open symbols) and  $1.5 < M/M_{\odot} \leq 3$  (filled symbols), with LOWESS regression curves.

these “effective” coronal temperatures, combined with those derived from the 1-T model fits, scale with the total X-ray luminosities as shown in Fig. 11c: the LOWESS result can be well approximated with the following linear relationship:

$$\log L_x = 27.6 + 3.0 \times \log T_{\text{avg}} \quad (1)$$

We have also investigated on the possible biases introduced by the differences in iron abundance on the distributions of the X-ray luminosity vs. temperature and vs. the ra-

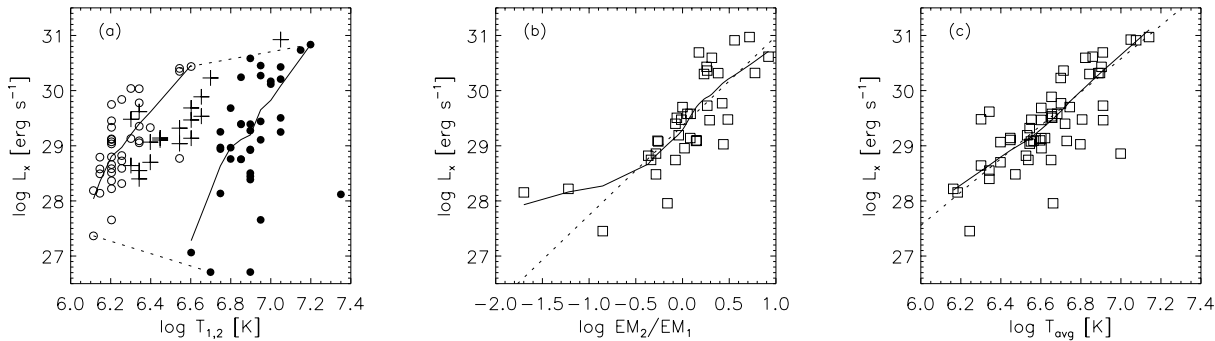


**Fig. 11.** **a** X-ray luminosities vs. temperature, for stars whose spectra have been fitted with 1-T models (plus symbols) or 2-T models (open and closed circles for the two components). Two dashed lines connect the components of the two stars with the lowest and highest total X-ray luminosity; the solid lines are the result of a LOWESS regression applied separately to the low- and high-temperature components (for 2-T model fits only). **b** X-ray luminosity vs. ratio of emission measures, for stars with 2-T model fits. The solid line has been obtained with a LOWESS regression, while the dotted line is a least-squares linear approximation to the LOWESS result, for  $EM_2/EM_1 > 0.1$ . **c** X-ray luminosity vs. average coronal temperature, with LOWESS regression (solid line) and linear approximation (dotted line).

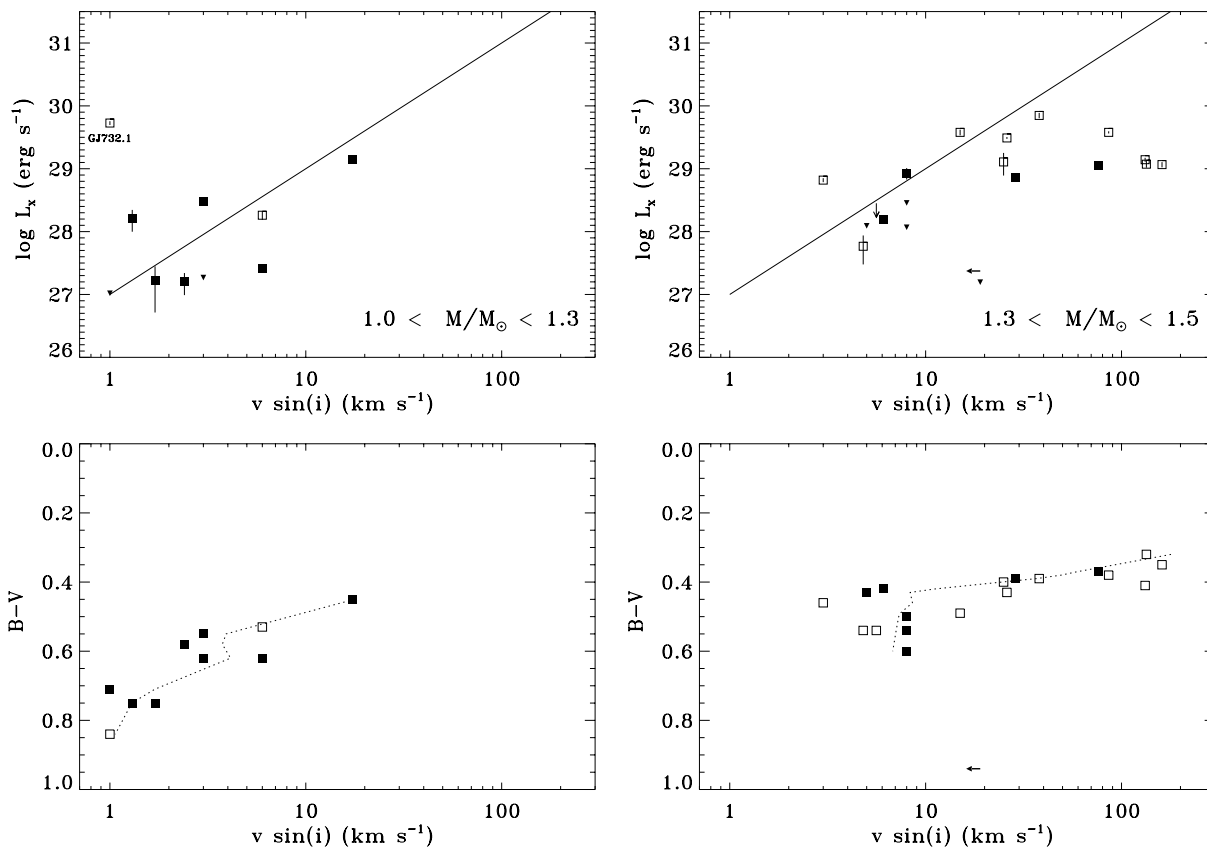


**Fig. 12.** Distributions of X-ray luminosities (or upper limits) vs.  $v \sin i$  for single and resolved binary stars (filled symbols) and unresolved binaries (open symbols), in the two mass ranges indicated on top of each panel (upper row). The bottom panels show the corresponding distributions in the  $B-V$  vs.  $v \sin i$  diagram. Note that the  $B-V$  axis has been inverted to ease inspection of the  $v \sin i$  vs.  $B-V$  decreasing trend, shown by the LOWESS regression (dotted line) applied to all stars in each mass range.

tio of the emission measures. We have performed the spectral fitting for all the stars in Fig. 11 using two different metallicities,  $[Fe/H]_{\odot} = -0.4$  and  $[Fe/H]_{\odot} = 0.2$ , corresponding to the 90% range of the photospheric Fe/H distribution (see Fig. 1), in order to check how the best-fit parameters change. We have found that *both* the emission measures associated to

the two thermal components decrease by factors 3–4 for increasing  $[Fe/H]_{\odot}$ , in such a way that their ratio becomes lower by  $\lesssim 30\%$  in going from the low to the high metallicity extreme. At the same time we have checked that variations of the average coronal temperature and of the X-ray luminosity computed by assuming different metal abundances are less than 5%. We

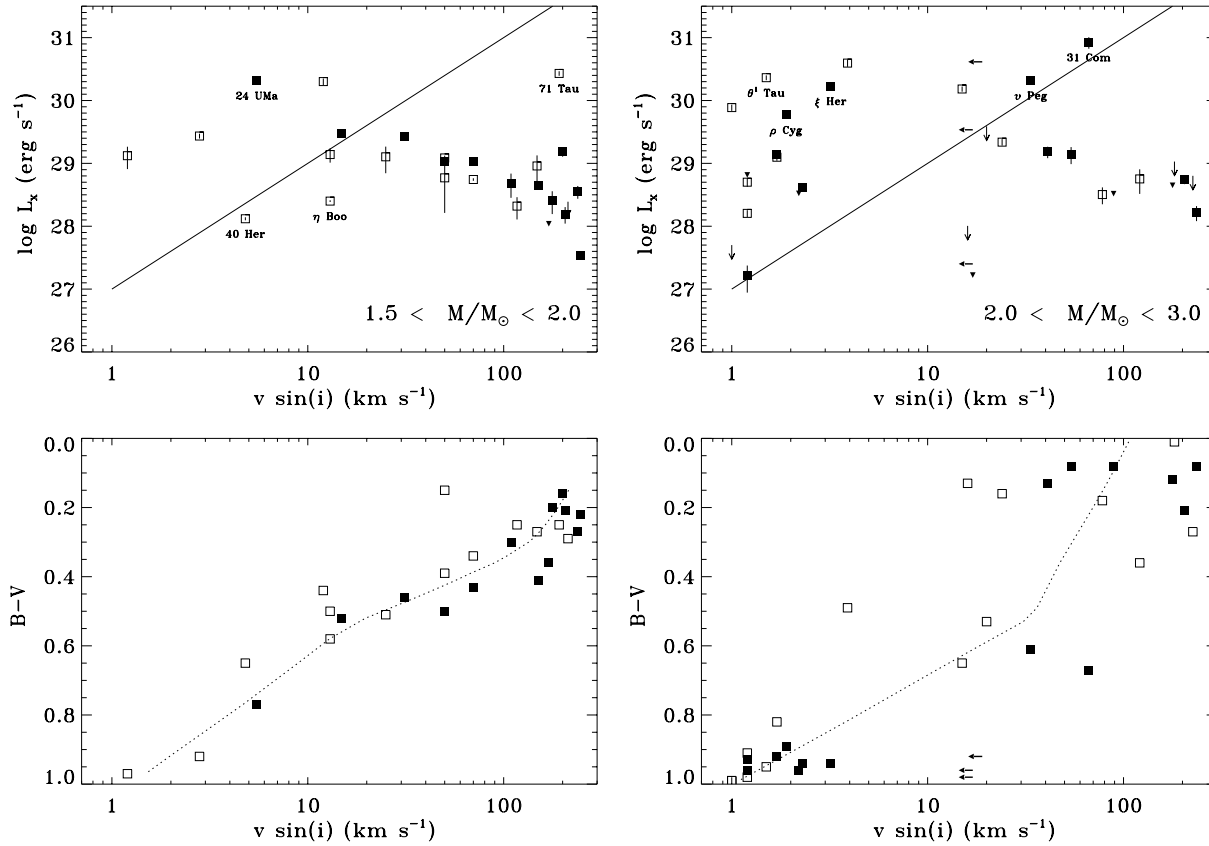


Fig. 13. Similar to Fig. 12, but for the two subsamples of intermediate mass stars.

conclude that the correlations noted above are not significantly affected by the assumed coronal metallicity.

The above results, together with those found in Sect. 3.1, suggest that – during stellar evolution – coronal temperatures and X-ray luminosities follow similar trends; in particular, the coronae of lower-mass stars ( $M < 1.5M_{\odot}$ ) tend to become cooler with advancing evolutionary phases, while for intermediate-mass stars ( $1.5 < M/M_{\odot} < 3$ ) higher X-ray emission levels correspond to hotter coronae.

### 3.3. Activity vs. rotation

In Fig. 12 and 13 we have plotted the distributions of X-ray luminosities vs.  $v \sin i$  and  $v \sin i$  vs. B-V, for single and binary stars in each of the mass ranges already considered. Different behaviors are evident also in these distributions, for stars in different mass ranges. In the upper plots we have also drawn a solid line representing the well-known Pallavicini et al. (1981) law  $L_x \propto (v \sin i)^2$ , in order to see how this law compares with the actual behavior of evolved stars. In practice, (a) stars with  $M/M_{\odot} < 1.3$  are loosely scattered around the Pallavicini’s law, with the exception of the suspected spectroscopic binary HD 175225 (GJ 732.1), having high X-ray luminosity in spite of a low projected rotational velocity, suggesting that it may be viewed nearly pole-on; (b) stars with  $1.3 < M/M_{\odot} < 1.5$  and  $L_x > 10^{29}$  erg s $^{-1}$ , having  $v \sin i > 20$  km s $^{-1}$  and B-V < 0.4,

show similar X-ray luminosities in spite of a factor 10 spread in rotational velocities, while the less X-ray luminous and redder stars are clustered close to the Pallavicini’s law; (c) stars with  $1.5 < M/M_{\odot} < 2.0$  show instead a trend of *decreasing* X-ray luminosity with *increasing* rotational velocity; (d) finally, among the stars with  $2.0 < M/M_{\odot} < 3.0$ , those bluer than B-V  $\sim 0.4$  show the same trend observed in the previous mass range, but most of the gap giants with  $0.5 < B-V < 0.8$ , like  $v$  Peg and 31 Com, are close to the Pallavicini’s law, and most of the stars redder than B-V = 0.8 rest well above the Pallavicini’s law.

On the other hand, all stars follow similar trends of decreasing rotational velocity for increasing B-V, in each mass range. Note in particular that the stars with B – V > 0.8 have similar low values of  $v \sin i = 1\text{--}4$  km s $^{-1}$  (whenever reliable measurements are available), but show a spread in X-ray luminosities of more than three orders of magnitude. On the basis of our previous results (Sect. 3.1), one can be tempted to identify the high X-ray luminosity stars ( $L_x > 10^{29}$  erg s $^{-1}$ , like  $\xi$  Her and  $\rho$  Cyg) with first-crossing evolved stars at the blue edge of the Hertzsprung gap, and the stars with lower X-ray luminosities with clump giants; unfortunately, this is a necessary but not sufficient condition for discriminating between the two classes of stars: in fact, there are well-known examples of true clump giants, like  $\theta^1$  Tau in the Hyades cluster or the field star  $\beta$  Cet (not

in our sample; see Maggio et al. 1998), which show high X-ray emission levels in spite of their low rotational velocities.

### 3.4. Close binaries

Finally, we have investigated the possibility of a connection between X-ray activity and mass in spectroscopic binaries with different orbital periods. Melo & De Medeiros (1996) noticed higher levels of X-ray emission in short-period spectroscopic binaries ( $\lesssim 100$  days) with respect to long-period binaries ( $\gtrsim 100$  days). In particular, these authors found, for binaries with  $P_{\text{orb}} \lesssim 100$  days, X-ray to visible flux ratios about two orders of magnitude higher than for longer period binaries. They argued that this behavior may be due to synchronization between orbital motion and rotation, caused by tidal effects, in the shorter period binary stars, and consequent enhancement of the magnetic activity. We have checked this result with our larger sample, retrieving from literature the values of orbital periods for 35 out of the 44 spectroscopic binaries (Batten et al. 1989; Strassmeier et al. 1993). For these binary systems we have plotted in Fig. 14 the X-ray to visible flux ratio vs. the orbital period, maintaining the distinction between stars with mass  $< 1.5M_{\odot}$  and stars with  $1.5 < M/M_{\odot} < 3.0$ . It appears that the trend noted by Melo and De Medeiros may be valid only for the lower-mass stars, while it is not followed by the more massive stars. This is somewhat surprising since their sample includes only late-G and early K giants with masses likely larger than 2–3  $M_{\odot}$ .

## 4. Discussion and conclusions

Our study confirms the existence of a different evolutionary behavior of X-ray activity for stars with  $M < 1.5M_{\odot}$ , which have spent most of their main sequence life as X-ray emitters, with respect to stars with  $1.5 < M/M_{\odot} < 3.0$  (A-type inactive stars on the main sequence). In particular, the X-ray luminosity of the lower-mass stars decreases, on average, during post-main-sequence evolutionary phases, while the intermediate mass stars show a trend of increasing emission levels with age. The behavior of the lower-mass stars is likely the consequence of their main-sequence lifetime, already spent as X-ray emitting sources, with a stellar dynamo generating strong magnetic fields and a braking mechanism affecting the stellar rotation, the efficiency of the dynamo and the coronal activity also in the subsequent evolutionary phases out of the main sequence. The behavior of the higher-mass stars is instead likely due to the effect of the changes in their internal structure on the magnetic dynamo efficiency. These fast-rotating but inactive stars on the main sequence develop an efficient magnetic dynamo already in early phases of their evolution across the Hertzsprung gap, thanks to the formation and deepening of a convective envelope.

Our results confirm the qualitative conclusions drawn from previous works (Maggio et al. 1990; Schröder et al. 1998), and emphasize the importance of studying the evolution of stellar activity considering stars in selected mass ranges. This approach

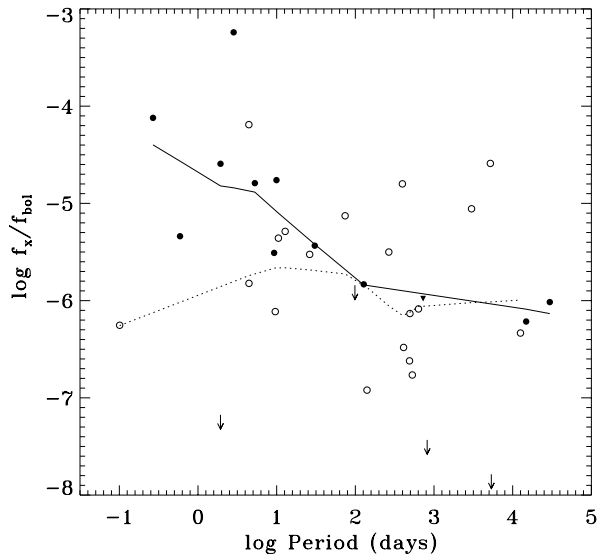


**Fig. 14.** Scatter plot of X-ray to visible flux ratio vs. the orbital period, for 35 spectroscopic binaries in our sample. Open and filled symbols refer to stars with  $M/M_{\odot} > 1.5$  and  $M/M_{\odot} < 1.5$ , respectively, and the dotted and solid lines are the corresponding LOWESS regression curves.

allows us to proceed – on firm grounds – with some comparison between observations and model predictions.

Schrijver & Pols (1993) have analyzed the observed rotation rates of subgiant and giant stars evolving from the main-sequence to the red giant branch, and compared them with predictions based on evolutionary models incorporating, in a parametric way, the core-envelope exchange of angular momentum and the stellar magnetic braking. They concluded that the loss of angular momentum inferred from the drop of the surface rotational velocities cannot be simply explained by changes in the stellar moment of inertia, but the action of a magnetic brake is required; however, the latter effect, and possibly the magnetic dynamo itself, does not switch on at full strength from the moment envelope convection sets in, but rather its efficiency appear to increase over an interval of at least  $\Delta(B-V) \sim 0.2\text{--}0.3$ .

Our results largely confirm their conclusions, in that we observe a steady increase of the X-ray luminosity (a tracer of the dynamo activity) for intermediate-mass stars crossing the Hertzsprung gap; however, such a trend occurs over a larger color range,  $\Delta(B-V) \sim 0.5\text{--}0.6$ , than suggested by their work.

A further conclusion drawn by Schrijver & Pols (1993) is that the rotational shear between the envelope and the interior is limited by the short time scale on which the core-envelope exchange of angular momentum occurs ( $t_c < 5$  Myr, for a  $2.5M_{\odot}$  giant), but quite high values of radial differential rotation could be achieved, up to  $\Delta_r\Omega/\Omega \sim 3$  for the longest allowed core-envelope coupling time.

In the framework of a solar-type linear  $\alpha$ - $\Omega$  dynamo, large amounts of differential rotation imply a strong  $\Omega$ -effect, i.e. a more efficient amplification of magnetic fields in the stellar interior, and hence higher levels of surface magnetic activity. This is indeed what we observe for some of the gap giants, like

24 UMa, and for most of the intermediate-mass stars at the exit of the Hertzsprung gap, whose X-ray luminosities can be two or three orders of magnitude higher than G dwarfs with comparable surface rotation rates (as indicated by the Pallavicini's activity-rotation law, in Fig. 13).

A similar interpretation can be derived from the theory of turbulence-induced differential rotation developed by Kitchatinov & Rüdiger (1995). According to this theory both the latitudinal and the radial differential rotation increase with decreasing rotation rate and/or convective turnover time. Kitchatinov & Rüdiger (1999) generated a sequence of differential rotation models for giants of  $2.5M_{\odot}$ , covering the evolutionary phases from about G2III to K1III. Assuming the mean angular velocities measured by Gray (1989), they found that the model-predicted differential rotation in giant stars is larger than for main-sequence stars of similar spectral type; moreover, their simulations predict an increase of the latitudinal differential rotation by a factor  $\sim 1.5$  during the evolutionary phases from G2III to K0III, and an increase of the radial differential rotation by a factor 3.5. On the other hand, the rotation laws are always solar-like, i.e. the angular velocity increases strongly from pole to equator, but varies relatively little with depth, suggesting similar magnetic activity characteristics in giants and in dwarfs.

The above arguments provide support to the hypothesis that a key ingredient for understanding the variation of the X-ray emission level for stars in post-main-sequence evolutionary phases is the stellar differential rotation.

The above scenario also explains, at least qualitatively, the relation between X-ray emission and rotation for evolved stars in different mass ranges. The trend for decreasing X-ray luminosities with decreasing rotation rates, followed by the low-mass subgiants, indicates that magnetic braking is the mechanism which controls the decay of the stellar dynamo also in post-main-sequence evolutionary phases (as well as in the preceding main-sequence lifetime), likely because it operates on time scales shorter than other effects relevant for the dynamo, due to modifications of the stellar internal structure and/or of the differential rotation profiles. Instead, the evolution of coronal activity in intermediate-mass stars is dominated by these latter effects, which cause the onset and growth of a very efficient dynamo on time scales comparable with the crossing time through the Hertzsprung gap, and with those required by the newborn magnetized winds to brake the star. As a consequence, we observe an increase of the coronal activity occurring simultaneously with a decrease of the rotation rate, i.e. the opposite of what occurs for main-sequence stars of similar spectral type.

Several issues need to be addressed by future researches: 1) how the growth rate of the stellar dynamo in intermediate-mass stars compares with the other evolutionary time scales? Is this rate fast enough to allow for a stellar dynamo evolution through *quasi-stationary* states? If so, what kind of dynamo is operating, and what global stellar parameters can be used, if any, for predicting the activity level during the evolution, including the coronal X-ray emission? In fact, all the classical parameterizations which have been employed for main-sequence stars, based

on rotation rates or Rossby numbers, may cease to be useful if a stationary state is not achieved.

Finally, the results of our spectral analysis show unambiguously that the increase in X-ray luminosity among the intermediate-mass evolved stars is accompanied, on average, by an increase of the coronal temperature, confirming early and more recent suggestions by Vaiana (1983) and by Maggio et al. (1994). Evidence for a correlation between the X-ray emission level and coronal temperatures (or its proxy, the spectral hardness ratio) has been already found for main-sequence stars (e.g. Schmitt et al., 1990; Preibish 1997; Schmitt 1997) and for the nearby evolved stars studied by Hünsch et al. (1996) and Reimers et al. (1996). The novelty of our results rests in the demonstration that the functional form of the relation between X-ray luminosity and temperature is indeed very nearly a power-law, and that the correlation holds also for stars of similar mass in different evolutionary phases.

*Acknowledgements.* The authors acknowledge partial support for this work from Agenzia Spaziale Italiana and Ministero dell'Università e della Ricerca Scientifica e Tecnologica.

## References

- Ayres T.R., Linsky J.L., Vaiana G.S., Golub L., Rosner R., 1981, ApJ 250, 293
- Ayres T.R., Fleming T.A., Schmitt J.H.M.M., 1991, ApJ 376, 45
- Ayres T.R., Fleming T.A., Simon T., et al., 1995, ApJS 96, 223
- Ayres T.R., Brown A., Harper G.M., et al., 1997, ApJ 491, 876
- Ayres T.R., Simon T., Stern R.A., et al., 1998, ApJ 496, 428
- Balachandran S., 1990, ApJ 354, 310
- Barnes T.G., Evans D.S., Moffett T.J., 1978, MNRAS 183, 285
- Batten A.H., Fletcher J.M., MacCarthy D.G., 1989, Publ. Dom. Astrophys. Obs. vol. 17, 1
- Brown J.A., Sneden C., Lambert D.L., Dutchover E., 1989, ApJS 71, 322
- Cayrel De Strobel G., Hauck B., Francois P., et al., 1992, A&AS 95, 273
- Cleveland W.S., 1979, Robust locally weighted regression and smoothing scatterplots. Journal of the American Statistical Association 74, 829
- Damiani F., Maggio A., Micela G., Sciortino S., 1997, ApJ 483, 370
- De Medeiros J.R., Mayor M., 1995, A&A 302, 745
- De Medeiros J.R., Do Nascimento J.D. Jr, Mayor M., 1997, A&A 317, 701
- De Medeiros J.R., Mayor M., 1999, A&AS 139, 433
- Duquenois A., Mayor M., 1991, A&A 248, 485
- Fekel F.C., 1997, PASP 109, 514
- Flower P.J., 1996, ApJ 469, 355
- Gondoin P., Mangeney A., Praderie F., 1987, A&A 174, 187
- Gondoin P., 1999, A&A 352, 217
- Gray D.F., 1989, ApJ 347, 1021
- Gunn A.G., Mitrou C.K., Doyle J.G., 1998, MNRAS 296, 150
- Hoffleit D., Warren W.H. Jr., 1991, The Bright Star Catalogue. 5th Revised Ed. (Preliminary Version)
- Hünsch M., Schmitt J.H.M.M., Schröder K.P., et al., 1996, A&A 310, 801
- Hünsch M., Schmitt J.H.M.M., Voges W., 1998, A&AS 127, 251
- Huebner W.F., Merts A.L., Magee N.H., Argo M.F., 1977, Los Alamos Sci. Lab. Rept., LA-6760-M

- Kitchatinov L.L., Ruediger G., 1995, *A&A* 299, 446  
Kitchatinov L.L., Ruediger G., 1999, *A&A* 344, 911  
Kurucz R.L., 1979, *ApJS* 40, 1  
Kurucz R.L., 1991, *Stellar Atmosphere-Beyond Classical Models*, 441  
Luck R.E., Challener S.L., 1995, *AJ* 110, 2968  
Mackie G., Fabbiano G., Harnden F.R. Jr., et al., 1996, In: Jacoby G.H., Barnes J. (eds.) *Astronomical Data Analysis Software and Systems V*, ASP Conf. Series 101, p. 179  
McWilliam A., 1990, *ApJS* 74, 1075  
Maggio A., Vaiana G.S., Haisch B.M., et al., 1990, *ApJ* 348, 253  
Maggio A., Sciortino S., Harnden F.R. Jr., 1994, *ApJ* 432, 701  
Maggio A., Favata F., Peres G., Sciortino S., 1998, *A&A* 330, 139  
Melo C.H.F., De Medeiros J.R., 1996, *A&A* 310, 797  
Pallavicini R., Golub L., Rosner R., et al., 1981, *ApJ* 248, 279  
Paresce F., 1984, *AJ* 89, 1022  
Preibisch T., 1997, *A&A* 320, 525  
Reimers D., Huensch M., Schmitt J.H.M.M., Toussaint F., 1996, *A&A* 310, 813  
Rogers F.J., Iglesias C.A., 1992, *ApJS* 79, 507  
Rosner R., Musielak Z.E., Cattaneo F., Moore R.L., Suess S.T., 1995, *ApJ* 442, 25  
Schaller G., Schaerer D., Meynet G., Maeder A., 1992, *A&AS* 96, 269  
Schmitt J.H.M.M., Collura A., Sciortino S., et al., 1990, *ApJ* 365, 704  
Schmitt J.H.M.M., 1997, *A&A* 318, 215  
Schrijver C.J., Pols O.R., 1993, *A&A* 278, 51  
Schröder K.P., Hüsch M., Schmitt J.H.M.M., 1998, *A&A* 335, 591  
Stepien K., 1994, *A&A* 292, 191  
Strassmeier K.G., Hall D.S., Fekel F.C., Scheck M., 1993, *A&AS* 100, 173  
Taylor B.J., 1994, *PASP* 106, 704  
Vaiana G.S., Fabbiano G., Giacconi R., 1981, *ApJ* 245, 163  
Vaiana G.S., 1983, *IAUS* 102, 165  
VandenBerg D.A., 1985, *ApJS* 58, 711